Taylor & Francis
Taylor & Francis Group

Check for updates

Light absorption and scattering properties of indole secondary organic aerosol prepared under various oxidant and relative humidity conditions

Vahe J. Baboomian[a] (ID), Quanfu He[b] (ID), Julia Montoya-Aguilera[a] (ID), Nabila Ali[a] (ID), Lauren T. Fleming[a] (ID), Peng Lin[c] (ID), Alexander Laskin[c] (ID), Julia Laskin[c] (ID), Yinon Rudich[b] (ID), and Sergey A. Nizkorodov[a] (ID)

[a]Department of Chemistry, University of California, Irvine, California, USA; [b]Department of Earth and Planetary Sciences, Weizmann Institute of Science, Rehovot, Israel; [c]Department of Chemistry, Purdue University, West Lafayette, Indiana, USA

ABSTRACT

Secondary organic aerosol (SOA) from indole was produced in a smog chamber under different relative humidity (RH = <2%, 25% and 50%) and with different oxidants (O_3, OH, $OH + NO_x$, and NO_3). The mass absorption coefficients were measured by extracting SOA in methanol and taking absorption spectra in the 200-700 nm range. Chromophoric compounds were tentatively identified by liquid chromatography – spectrophotometry – mass spectrometry. One of the strongest chromophores was nitroindole, produced in high abundance by both NO_3 and $OH + NO_x$ oxidation. Indole SOA was also prepared in an oxidation flow reactor (OFR) using the same set of oxidants under variable RH conditions. Densities of the OFR-generated SOA particles ranged from 1.05 g/cm^3 for indole + O_3 SOA to 1.33 g/cm^3 for indole + OH SOA. The real (n) and imaginary (k) refractive indices were quantified using a broadband cavity-enhanced spectrometer (BBCES) over the 360–425 nm spectral range. The values of k ranged from 10^{-2} to 10^{-1} at 405 nm, which is comparable to those for humic-like substances and at least an order of magnitude larger than k values of SOA produced from other biogenic and anthropogenic volatile organic compounds. The k values for the indole + NO_3 SOA had a strong and non-monotonic dependence on RH, suggesting two competing reaction mechanisms for the chromophores, highlighting the complex effect of water on the absorption coefficient of SOA from heterocyclic aromatic precursors. Strong absorption of indole SOA may contribute to the degradation of visibility near its emission sources, which include animal husbandry facilities and stressed plants.

1. Introduction

Atmospheric particulate matter absorbs and scatters incoming solar radiation, which has important implications for air quality, visibility and climate change (Chen 2021). Secondary organic aerosol (SOA) accounts for a considerable fraction of airborne particulate matter (Hodzic et al. 2016) and is largely formed through the oxidation of biogenic and anthropogenic volatile organic compounds (VOCs), followed by gas-particle partitioning of the low volatility oxidation products (Hallquist et al. 2009). Aqueous phase processing of organic compounds can also add to the SOA burden in the atmosphere, where water-soluble volatiles are taken up into the particle phase and are then oxidized to form low-volatility products (Herrmann et al. 2015).

Brown carbon (BrC) is defined as the aerosol organic matter that strongly absorbs solar radiation across the near-UV (300-400 nm) and visible ranges (Andreae and Gelencser 2006; Laskin, Laskin, and Nizkorodov 2015; Moise, Flores, and Rudich 2015; Saleh 2020). While BrC is not as light-absorbing as black carbon, there is enough BrC in the atmosphere to measurably reduce the single scattering albedo and contribute to the radiative forcing of climate by aerosols. Examples of BrC include primary organic aerosol (POA) produced by biomass burning (Hettiyadura et al. 2021; Lack et al. 2013; Li et al. 2020a; Li et al. 2020b; Samburova et al. 2016) and SOA generated by photooxidation of polycyclic aromatic compounds (He et al. 2022; Lin et al. 2015; Liu et al. 2015; Siemens et al. 2022). It is important to identify major BrC sources, both primary and secondary, to more accurately predict the effect of BrC on visibility and climate.

Indole is a heterocyclic nitrogen-containing VOC emitted by certain plants during stress and flowering events when its emissions become substantial. For example, in the San Joaquin Valley, an agricultural region in California, indole was measured at levels as high as $4.7–18 \mu g \ m^{-3}$, which was comparable to or greater than concentrations of myrcene, a dominant monoterpene (Gentner et al. 2014). Once emitted, indole plays an important role in plant ecology, for example, by attracting pollinators (Zito, Dotterl, and Sajeva 2015). Another important source of indole is the microbial processing of L-tryptophan in the intestines or feces of livestock animals (Le et al. 2005). The ranges of emission rates and concentrations of indole detected in swine facilities or during the land application of swine slurry are $0.13–2.67 \mu g \ m^{-2} min^{-1}$ (Le et al. 2005; Parker et al. 2013) and $0.07–500 \mu g \ m^{-3}$ (Hobbs, Misselbrook, and Pain 1997; Jo et al. 2015; Osaka, Miyazaki, and Tanaka 2018), respectively. For decades, indole and its derivatives have been utilized in agricultural applications and in consumer products. One of the better-known derivatives of indole is indigo dye (also known as indigotin) (Baeyer and Drewsen 1882), which is still used to dye jeans to their characteristic deep blue color. With the increasing recognition of the role of consumer products in air pollution (Coggon et al. 2021; McDonald et al. 2018), it is important to investigate the atmospheric chemistry of indole and other heterocyclic aromatic VOCs.

The oxidation of indole by OH has been previously shown to produce highly-absorbing SOA, in which dimeric products of indole oxidation, such as tryptanthrin, indirubin, indigo dye, and indoxyl red, were largely responsible for the absorption (Montoya-Aguilera et al. 2017). The indole + OH SOA reaction has been incorporated into a model to simulate its effects on the air quality in the South Coast Air Basin of California, USA. This model showed that absorption by the indole-derived BrC is not likely to compete with black carbon (BC) in urban areas but may contribute to visibility reduction in remote areas with lower BC contribution. Moreover, the model suggested that indole oxidation by NO_3 may lead to higher nighttime SOA concentrations (Montoya-Aguilera et al. 2017), resulting in a sustained increase in SOA concentration throughout the day. However, the effect of indole + NO_3 SOA on atmospheric extinction could not be modeled because the light absorption properties of this SOA were unknown at the time. The first objective of this work is to study indole oxidation by the most important atmospheric oxidants (OH in the absence and presence of NO_x, O_3 and NO_3), thus providing valuable data for modeling the effects of indole on climate forcing and visibility.

The second objective of this work is to explore the effects of relative humidity (RH) on the BrC properties of indole SOA. The absorption coefficient of organic aerosols appears to be quite sensitive to their chemical composition because it is controlled by a handful of chromophores (Laskin, Laskin, and Nizkorodov 2015). Recent studies have demonstrated that the absorption coefficient of SOA produced from aromatic (Cui et al. 2021) and heterocyclic aromatic compounds is RH-dependent (Kasthuriarachchi et al. 2020). A strong effect of RH was recently reported for optical properties of toluene SOA produced under high-NO_x conditions (Mitra et al. 2022). In this study, we report a complex effect of RH on the absorption coefficient of indole SOA, suggesting at least two distinct competing mechanisms for BrC production from indole.

2. Methods and materials

2.1. Smog chamber SOA generation

Indole SOA was generated in a $5 \ m^3$ Teflon chamber at different levels of RH (<2%, 25%, 50%), which was measured by a HMT333 probe (Vaisala Inc., Finland). No inorganic seed aerosol was used to avoid interference with the off-line mass-spectrometric analysis of SOA. Indole (99% purity, Sigma-Aldrich) was dissolved in methanol (LC-MS grade, 99.9% purity, Honeywell) and evaporated into the chamber to obtain an initial mixing ratio of 200 ppb, which is equivalent to $960 \mu g \ m^{-3}$. The injector and inlet lines were heated to $70 \degree C$ to minimize losses of indole on the injector surfaces. While 200 ppb of indole was used in most experiments to collect sufficient mass for analysis, several experiments were done at lower mixing ratios (50 ppb and 100 ppb) to test the dependence of indole SOA optical properties on the starting indole mixing ratios (see Figure S1). In the nitrate radical experiments, NO_3 was generated in the chamber by introducing O_3 and NO in a small excess of the 2:1 ratio (500 ppb O_3 and 200 ppb NO). Under these conditions, 200 ppb NO is expected to convert to ~200 ppb NO_3 (a fast conversion of NO to NO_2 followed by slower conversion of NO_2 to NO_3 but still only taking a few seconds), with ~100 ppb of residual ozone. Because NO_3 is much more reactive toward indole than O_3, with rate constants of $1.3 \times 10^{-10} cm^3$ $molec^{-1}$ s^{-1} for indole + NO_3 compared to $5 \times 10^{-17} cm^3$ $molec^{-1}$ s^{-1} for indole + O_3 (Atkinson

et al. 1995), indole primarily reacts with NO_3 under these conditions. The ozonolysis experiments were conducted in the presence of 1 ppm O_3. In the OH photooxidation experiments, hydrogen peroxide was introduced into the chamber by evaporation of a 30 wt% solution of H_2O_2 in water (Fisher Scientific) into a clean air flow to achieve an initial mixing ratio of 2 ppm. UV-B lamps (FS40T12/UVB, Solarc Systems, Inc.) were turned on to initiate the photooxidation, which led to [OH] concentration of $\sim 1.4 \times 10^6$ molecules cm^{-3}. Table 1 summarizes SOA preparation conditions for the chamber experiments.

Throughout the experiment, the particle size distribution was monitored with a scanning mobility particle sizer (SMPS; TSI 3936) equipped with a condensation particle counter (CPC; TSI 3775). A proton-transfer-reaction time-of-flight mass spectrometer (PTR-ToF-MS; Ionicon model 8000) monitored the decay of indole, as well as the formation of volatile products. The PTR-ToF-MS had a resolving power of m/Δm $\sim 5 \times 10^3$ and was operated with the following settings: drift tube temperature of 60 °C, drift tube voltage of 600 V, normalized electric field strength of E/N $\sim$135 Td (1.35×10^{-15} V cm^2), and inlet flow of 0.2 SLM. When SOA reached a peak concentration in the chamber, UV irradiation was stopped, and the polydispersed particles were collected on a Teflon filter (47 mm diameter, Millipore FGLP04700) at 20 L min^{-1} for 2 h. One filter was collected per chamber run. Replicate samples were collected from separate experiment runs under the same conditions. The amount of the collected SOA material on each filter was determined by weighing using a microbalance (Sartorius ME5F, ± 1 μg precision) after letting the filter sit under laboratory RH conditions ($\sim$50% RH) to reduce the effects of the filter and SOA bound water. The material collected on the filter was assumed to contain only organic compounds. Under the OH + NO_x and NO_3 oxidation conditions, some nitric acid will be produced in the chamber. However, we

do not expect inorganic nitrates to partition in SOA as neither indole nor its major oxidation products are basic. The color of SOA collected on the filter was dependent on the oxidant and amount of SOA collected (0.5–2.5 mg), and was brown, yellow-green, or even black in appearance. Examples of filter photographs are given in the SI section (Figure S2). Visibly, the indole + NO_3 SOA appeared to be darker in color than indole + OH SOA or indole + O_3 SOA.

2.2. SOA MAC and k values

The weighted filters were extracted in 5 mL of methanol (LC-MS grade, 99.9% purity, Honeywell) and shaken on a shaker for 5 min. The filter color changed from colored to white suggesting most of the light-absorbing compounds were extracted. Furthermore, the UV absorbance of the extract after the first extraction was at least a factor of 20 larger than that after the second extraction (Figure S3). Since we can reasonably expect that all indole oxidation products that retain one or both aromatic rings must have strong $\pi \rightarrow \pi^*$ absorption bands in the UV range, we can conclude that the initial extraction dissolved >95% of the SOA compounds, permitting the calculation of the solution mass concentration, C_{mass} (g cm^{-3}) from gravimetric measurements. The SOA methanol extract was analyzed by ultraviolet-visible (UV-Vis) spectrophotometry using a dual beam Shimadzu UV-2450 instrument, with pure methanol used as reference. Mass absorption coefficients (MAC) of the SOA material were calculated as a function of wavelength (λ) from the measured base-10 absorbance, $A_{10}^{solution}(\lambda)$, the path length, $b = 1$ cm, and C_{mass}:

$$MAC\ (\lambda) = \frac{A_{10}^{solution}(\lambda)\ \times \ln(10)}{b\ \times\ C_{mass}} \quad (1)$$

The imaginary part of the refractive index, k, which describes the absorptive properties of the particle material was calculated from MAC values using Equation (2).

Table 1. SOA production conditions in both the smog chamber and the oxidation flow reactor (OFR). The starting mixing ratios and estimated OH concentrations are listed.

SOA Production Method	Oxidant	Indole (ppb)	NO (ppb)	NO_x (ppb)	O_3 (ppb)	OH (molec cm^{-3})	N_2O_5 (ppb)	RH values
Chamber	OH	200	–		–	1.4×10^6	–	<2%, 25%, 50%
Chamber	NO_3	200	200		500	–	–	<2%, 25%, 50%
Chamber	O_3	200	–		1000	–	–	<2%, 25%, 50%
Chamber	OH + NO_x	200	200		–	1.4×10^6	–	<2%
OFR	OH	200	–			2.3×10^9	–	38%
OFR	OH + NO_x	200	–	130		2.3×10^9	–	38%
OFR	OH + NO_x	200	–	670		2.3×10^9	–	38%
OFR	OH + NO_x	200	–	2400		1.7×10^9	–	38%
OFR	O_3	200	–	–	20000	–	–	<2%
OFR	NO_3	200	–	–	–	–	1000	<2%, 25%, 51%, 76%
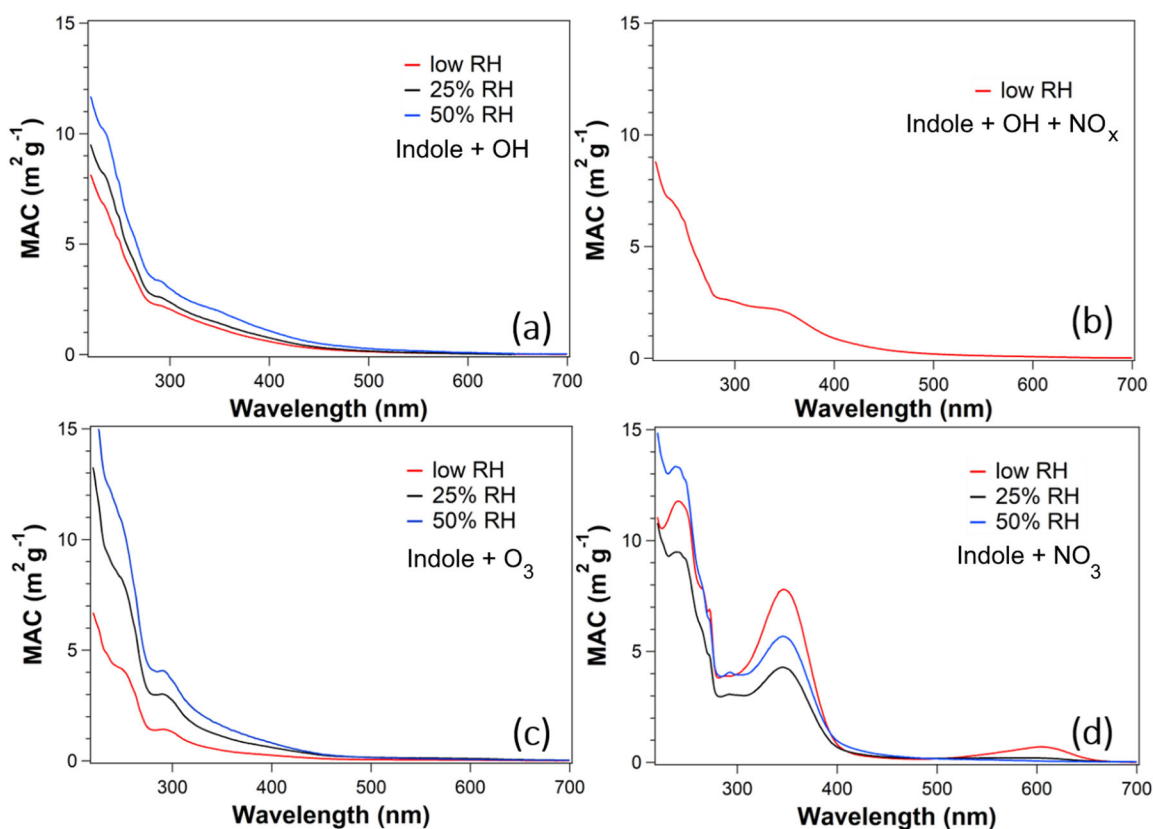
Figure 1. Wavelength-dependent mass absorption coefficients (*MAC*) of (a) indole + OH SOA, (b) indole + OH + NO$_x$ SOA, (c) indole + O$_3$ SOA, and (d) indole + NO$_3$ SOA generated at different RH. Only low relative humidity (<2% RH) data are available for the indole + OH + NO$_x$ conditions.

$$k\ (\lambda) = \frac{MAC\ (\lambda) \times\ \rho\ \times \lambda}{4\pi} \qquad (2)$$

We used the average measured effective density of $\rho = 1.21\,\text{g cm}^{-3}$, as discussed below. The estimated uncertainty in *MAC* is limited by the uncertainty of gravimetric measurements and completeness of extraction, and is likely to be below 20%. The uncertainty in *k* is somewhat higher because of the use of average density instead of the actual density (which was not measured for the smog-chamber generated SOA), but it is likely to be below 25%.

2.3. Chromophore identification

Additional SOA sample filters were collected for high performance liquid chromatography – photo diode array spectrophotometry – high resolution mass spectrometry (HPLC-PDA-HRMS) measurements as described previously (Montoya-Aguilera et al. 2017), for which one-quarter of the filter was extracted using 350 µL acetonitrile (CH$_3$CN, gradient grade, ≥99.9% purity). The completeness of extraction of light-absorbing compounds was confirmed by visual inspection of the filter, which returned to the white color of

a clean filter after the extraction. The first set of experiments used a Scherzo SM-C$_{18}$ column (Imtakt USA) for HPLC separation (referred to as Column A). Solvents A and B used during liquid chromatography were HPLC grade acetonitrile and water, respectively. The gradient elution protocol included a 3 min hold at 10% solvent A, a 45 min linear gradient to 80% solvent A, a 16 min hold at this level, a 1 min return to 10% solvent A, and another hold until the total scan time of 90 min. The column was maintained at 25 °C. The UV–Vis spectra of the eluted fractions of SOA were measured with a PDA detector from 250 to 700 nm. The electrospray ionization (ESI) settings in the positive ionization mode were +4.5 kV spray potential, 35 units of sheath gas flow, 8 units of auxiliary gas flow, and 5 units of sweep gas flow. The Thermo LTQ Orbitrap high resolution mass spectrometer was operated at a mass resolving power of $\sim 10^5$ at *m/z* 200. The HPLC-PDA-HRMS analysis was done as described in (Lin et al. 2016; Montoya-Aguilera et al. 2017).

An additional set of HPLC-PDA-HRMS experiments was performed two years later (the delay was due to the COVID-19 disruptions of 2020-21) using a different instrument configuration. These experiments
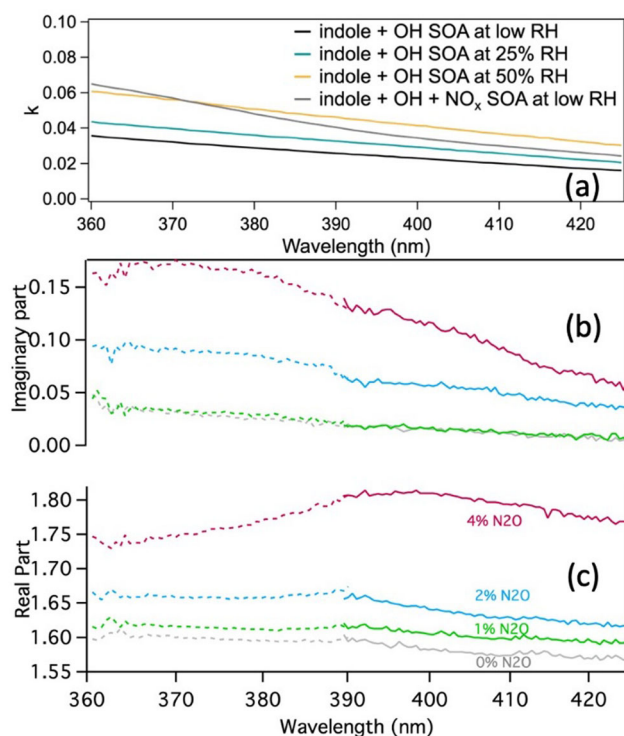
Figure 2. (a) k values calculated from *MAC* of indole + OH SOA prepared in a chamber under low and high NO$_x$ conditions. Measured (b) k and (c) n for indole SOA generated in an OFR under varying mixing ratios of N$_2$O (0-4%) and under dry conditions. The dotted and solid traces were collected using the BBCES in the 360–390 nm and 385–425 nm channels, respectively.
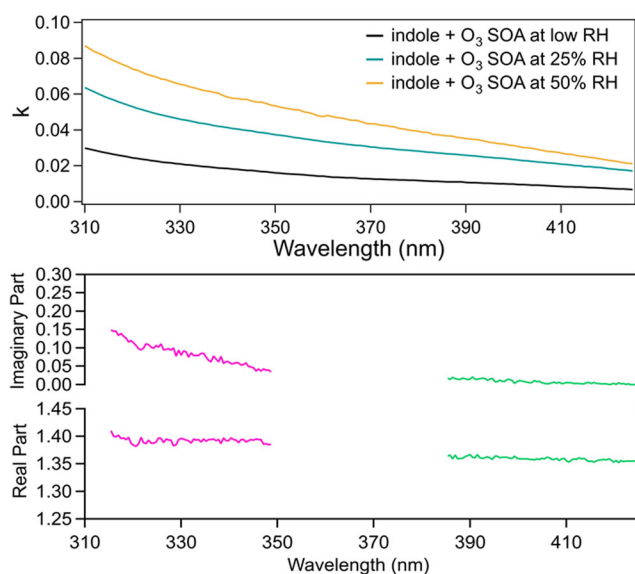
Figure 3. (a) k values calculated from *MAC* of indole + O$_3$ SOA prepared in a chamber under different RH (<2, 25 or 50%). Measured (a) k and (b) n for indole + O$_3$ SOA generated in a glass OFR under dry conditions. The gap in the bottom panel is due to the range of the BBCES system used for these experiments (315–345 and 380–700 nm).

utilized ultra-performance liquid chromatography coupled with a Thermo Q-Exactive Plus Orbitrap mass spectrometer equipped with an ESI source. Filters were extracted using a solvent consisting of 1:1 (v/v) mixture of acetonitrile (Sigma Aldrich, purity $\geq$ 99.9%) and water (Sigma-Aldrich, HPLC grade). A Luna 1.6 µm Omega Polar C$_{18}$ (150 × 2.1 mm) column was used for separation (referred to as Column B). Solvents A and B, which were used for mobile phase, were HPLC-grade acetonitrile (with 0.1% formic acid) and water (with 0.1% formic acid), respectively. The gradient elution protocol included a 3 min hold at 5% solvent A, an 11 min linear gradient to 95% solvent A, a 2 min hold at this level, and a linear gradient back to 5% solvent A in preparation for the next run. The column was maintained at 30 °C. The UV–vis spectra were measured with a PDA detector from 250 to 700 nm. The ESI settings in the positive ionization mode were +4.0 kV spray potential, 35 units of sheath gas flow, 10 units of auxiliary gas flow, and 8 units of sweep gas flow. The instrument was operated in the positive ion mode with a mass resolving power of ~10^5 at *m/z* 200. Data analysis was conducted using MZmine 2.53 software package (Pluskal et al. 2010). Molecular formulas were assigned to detected signals ($[M + H]^+$) satisfying the following constraints: C$_{1\text{-}40}$H$_{0\text{-}80}$O$_{0\text{-}35}$N$_{0\text{-}5}$ with a mass tolerance of 0.001 Da; element count heuristics $0.3 \leq H/C \leq 3$; $N/C \leq 4$, and $O/C \leq 3$.

2.4. Oxidation flow reactor experiments

Oxidation flow reactor (OFR) experiments were conducted for direct measurements of the optical properties of airborne indole SOA. SOA was generated at four different OFRs settings to simulate indole oxidation initialed by OH radical (with and without NO$_x$), O$_3$, and NO$_3$ radical. No seed aerosol was used in the OFR experiments. The experimental system is described in detail in previous publications (He et al. 2018; He et al. 2021). The OFR conditions used are summarized in Table 1.

Briefly, a potential aerosol mass (PAM) OFR was used for OH-initiated oxidation. Pure indole (99% purity, Sigma-Aldrich) was placed in a bubbler and was introduced into the PAM by a gentle N$_2$ flow to obtain an estimated initial mixing ratio of 200 ppb. For the SOA generation through OH oxidation, a total flow of 4.2 L min^{-1} of N$_2$ and 0.3 L min^{-1} O$_2$ at RH of 36 − 38% was used in the PAM with a corresponding residence time of 184 s. The OH concentration was controlled by changing the UV light intensity. To

simulate SOA formation in the presence of NO_x, 1%, 2%, and 4% N_2O were added to the PAM chamber as a NO_x source (Lambe et al. 2017), with corresponding NO_x concentrations of 0.13, 0.67, and 2.4 ppm measured at the exit of the OFR (Model T200, Teledyne, USA). Most of the measured NO_x is expected to be present in the OFR in the form of NO_2 but some NO_3 can be produced under OFR conditions, complicating the interpretation of our data. Using a simplified box model including the rate constants for the indole + OH, NO_3, and O_3 reactions, we estimated the average NO/NO_2 ratios of 0.0077, 0.011, and 0.0096, and the average OH/NO_3 ratios of 0.10, 0.078, 0.059 at the 1%, 2%, and 4% N_2O cases, respectively. However, the model predicts that most of the indole is oxidized within seconds of being added to the reactor, when the chemistry is still dominated by OH + NO/NO_2, and not by NO_3 oxidation. The OH exposures were regulated to $\sim 4.2 \times 10^{11}$ molecules cm^{-3} s, which were determined by measuring the decay of the SO_2 (Model 49i, Thermo Fisher Scientific, USA). Due to the limitation of the lamp power, the OH exposure was limited to $\sim 3.1 \times 10^{11}$ molecules cm^{-3} s for the experiments conducted with 4% N_2O.

SOA generation from ozonolysis of indole under dry (<2% RH) conditions was performed in a glass bulb OFR (20 L in volume) with an initial O_3 concentration of 20 ppm. A high O_3 concentration was used due to the low reactivity of indole toward ozone and a short residence time in the glass reactor (~ 20 min at the total flow of 1.0 L min^{-1}). To simulate NO_3 oxidation of indole, N_2O_5, synthesized ahead of time from the NO_2 reaction with ozone, was used as the source of the NO_3 radical in the same glass bulb OFR. The NO_3 radical was produced by thermal decomposition of N_2O_5, which was carried out by pure nitrogen flow from an N_2O_5 crystal cold trap. SOA production was achieved in a glass tube OFR (OFR, L:70 cm, ID: 7 cm), where N_2O_5 (~ 1 ppm) and the other gases were mixed. Particles were produced by homogeneous nucleation and condensation following NO_3 oxidation. The RH in the OFR was set to <2%, 25%, 51%, and 76% to examine the effect of RH on aerosol optical properties.

The complex refractive index of the aerosols, where the imaginary component k represents light absorption and the real component n represents scattering, was retrieved by measuring the extinction cross-section of size-selected particles and followed by fitting a theoretical Mie curve to the measured extinction cross-sections at each specific wavelength (Lang-

Yona et al. 2009; Riziq et al. 2007; Washenfelder et al. 2013). The aerosol flow from the OFR was sent through a VOC denuder and a drier, then size-selected with an aerosol aerodynamic classifier (AAC, Cambustion, UK) without charging the particles. The size-selected particles were then directed into the broadband cavity-enhanced spectrometer (BBCES) system (two broadband channels which span the 360–390 and 385–425 nm spectral regions) to measure the optical cross-section of the particles. The efficiency of size-selection was verified by measuring the size distribution with an SMPS, which measured sharp monodispersed selected particles (~ 130 nm). The BBCES system (He et al. 2018), that spans the wavelength range of 315–345 and 380–700 nm was employed for measuring the light extinction of particles from the O_3 oxidation of indole.

The chemical composition of the OFR-generated SOA particles was probed online with a Time-of-Flight Aerosol Mass Spectrometer (ToF-AMS), and the data was analyzed using SQUIRREL 1.62 A software with PIKA 1.22 A. For all the experiments, the particle size distribution was monitored by the SMPS.

3. Results and discussion

3.1. Particle densities and elemental ratios

Particle densities are necessary for calculating the imaginary refractive index of the SOA material from solution absorbance. Assuming that the SOA particles are spherical and non-porous, the particle effective densities can be calculated by comparing the aerodynamic diameter ($d_{Aero,}$ obtained from the AAC) and the mobility diameter (measured by SMPS):

$$\rho_{eff} = \frac{d_{aero}}{d_m} \times \rho_0 \tag{3}$$

The resulting densities of SOA particles produced in the OFR varied from 1.05 g/cm^3 for O_3 oxidation to 1.33 for low-NO_x OH oxidation (Table S1). This is comparable to densities of known indole oxidation products: isatin (1.47 g/cm^3), anthranilic acid (1.40 g/cm^3), indigo dye (1.20 g/cm^3), isatoic anhydride (1.52 g/cm^3), and 3-oxindole (1.20 g/cm^3). Our previous study of indole + OH SOA (Montoya-Aguilera et al. 2017) assumed a higher density of 1.4 g/cm^3, which means we slightly underestimated the yield of indole SOA and overestimated the MAC values reported in that work. In view of the relatively narrow spread of the densities measured for OFR SOA (Table S1), we elected to use the average of the measured effective densities (1.21 g/cm^3) to calculate k from

MAC of chamber-generated SOA using Equation (2). The uncertainty in *MAC* and *k* introduced by using this assumption is below 15%.

The elemental ratios of SOA particles produced in the OFR are listed in Table S1. For the indole + O_3 SOA, the N/C ratio of 0.112 is comparable to the N/C ratio in the indole itself (C_8H_7N, N/C = 0.125) suggesting that the products are likely dominated by the functionalized indole rather than its decomposition products. The indole + NO_3 SOA have slightly higher ratios ranging from 0.114 to 0.119, which is consistent with the expected nitration of the indole ring in some of the products. The O/C ratio of ∼0.5 for the indole + NO_3 SOA, is higher than that expected for nitroindole ($C_8H_7N_2O_2$, O/C = 0.25), suggesting that the products must contain additional oxygen-containing functional groups, such as hydroxyl or carbonyl. The indole + OH + NO_x SOA has the strongest dependence of the elemental ratios on the reaction conditions: the O/C ratios decrease from ∼1 to ∼0.7, and N/C ratios increase from 0.109 to 0.130 as the fraction of N_2O in the OFR increases from 1% to 4%. This points to a rather significant change in oxidation regime with the increased NO_x level. In the absence of the detailed mechanism of indole oxidation, we have not been able to model this behavior, but it is likely that high concentrations of NO_2 leads to direct reactions between OH-indole adducts (commonly formed in the OH oxidation of aromatic compounds) with NO_2 instead of oxygen.

3.2. Dependence of the mass-absorption coefficient on the oxidant and relative humidity

Figure 1 shows the *MAC*(λ) values of indole SOA samples prepared under different oxidation and RH conditions. Indole itself has several absorption bands between 200–290 nm, but its absorption coefficient is negligible in the near-UV and visible spectra range (Friedel and Orchin 1951). In contrast, the *MAC*(λ) spectra for indole SOA prepared under all smog chamber conditions extend into the visible range, similar to absorption spectra of common brown carbon aerosols (Laskin, Laskin, and Nizkorodov 2015). However, there are striking differences between the spectra. For example, the peak at 350 nm (Figure 1d) is a prominent feature in the indole + NO_3 SOA spectrum. Based on chemical analysis (see below), this peak is attributed to nitroindole ($C_8H_6N_2O_2$), which is a significant finding because only a single nitration step is required to produce this strong near-UV

absorber from indole. The 350 nm peak is also observable in the indole + OH + NO_x SOA (Figure 1b) but absent for the indole + O_3 (Figure 1c) and indole + OH SOA (Figure 1a) systems, which is fully consistent with its assignment to nitroindole. Another striking difference is the significant abundance of indigo dye distinguished by its characteristic absorption band at 600 nm (Weinstein and Wyman 1956) in the indole + NO_3 SOA prepared under <2% or 25% RH. The indigo dye peak is the strongest under dry conditions but becomes much weaker at 50% RH. It is also present in indole SOA prepared by OH and O_3 oxidation, but it is smaller in abundance than in the indole + NO_3 SOA.

The *MAC* values from Figure 1 were used to calculate the imaginary refractive index values using Equation (2) for chamber-generated SOA (Figures 2–4a) and compared to the *k* values obtained using BBCES for OFR-generated SOA (Figures 2–4b). We do not expect the *k* values between the two measurement methods to be the same because of different SOA formation conditions. For example, the indole + OH particles probed in the BBCES setup are more oxidized (i.e., aged) than in the smog chamber,
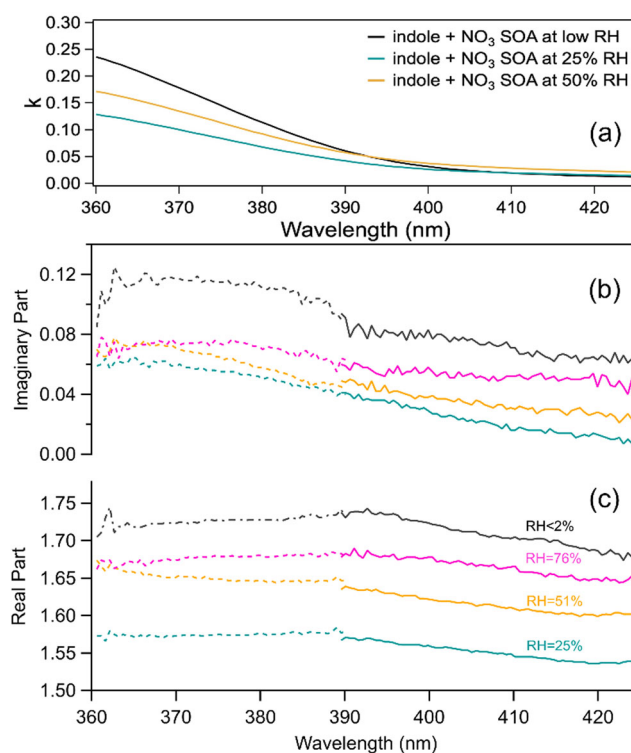
Figure 4. (a) *k* values calculated from MAC of indole + NO_3 SOA prepared in a chamber under different RH (<2, 25 or 50%). Measured (b) *k* and (c) *n* for indole + NO_3 SOA generated in a glass OFR reactor at various RH (<2%, 25, 51, 76%). The dotted and solid traces were collected using the BBCES in the 360–390 nm and 385–425 nm channels, respectively.

with OH exposures of $3.1 \times 10^{11} - 4.2 \times 10^{11}$ molecules cm^{-3} s and 1.5×10^{10} molecules cm^{-3} s, respectively. This difference in oxidation likely corresponds to differences in chemical composition and chromophores present. The differences in the measurement approach (BBCES vs. UV-Vis) may also contribute to the differences in k values. BBCES measures optical properties of the actual SOA material in aerosolized particles, whereas the UV-Vis method measures a spectrum from dissolved SOA material. For example, strong solvatochromic effects were observed in the indigo dye spectra with large peak shifts between the spectra recorded in solution and in the solid phase (Weinstein and Wyman 1956). Nonetheless, the k values obtained from the two independent methods are of the same order of magnitude, suggesting the effects of oxidation and SOA preparation methods on the k values and the solvatochromic shifts are relatively small in this case.

The *MAC* values can also be used to calculate the Absorption Ångström Exponent (*AAE*), an empirical parameter used to describe the wavelength dependence of the absorption coefficient. The resulting values of *AAE* ranged from 4.9 to 6.5 (Figure S4). (Saleh 2020) classified the strength of absorption by BrC based on the values of $w = AAE$-1 and k at 550 nm (at the peak of the solar spectrum). Based on the magnitude of the k values, indole SOA falls in between "very weakly absorptive BrC" (VW-BrC) and "weakly absorptive BrC" (W-BrC). However, the *AAE* values of indole SOA are lower than those typically observed for W-BrC (5-8) (Saleh 2020) (Figure S5), making its absorption spectrum overlap better with the solar spectrum.

Indole + OH SOA k values increase with increasing RH (Figure 2a) and with increasing amounts of NO_x (Figure 2b and c). The RH dependence of k for indole + O_3 SOA (Figure 3) has the same trend as the photooxidation samples (Figure 2): the k values generally increase with increasing RH.

Unlike SOA prepared by photooxidation or ozonolysis, the k values for indole + NO_3 SOA do not have a monotonic dependence on RH (Figure 4), both in smog chamber and OFR data. Instead, the k values for indole + NO_3 SOA are highest for SOA prepared under dry conditions (<2% RH), then decrease at 25% RH, and subsequently increase at 50% RH, a trend captured by both experimental methods (Figures 4a–c). This non-monotonic RH dependence can also be seen when considering the RH dependence of individual chromophores that form in SOA under different conditions, as discussed below. We note that a similar non-monotonic dependence of absorption coefficient on RH was recently reported for toluene + OH/NO_x SOA (Mitra et al. 2022).

Overall, the k values reported here are remarkably high, even at visible wavelengths. For example, at 405 nm, which is a common wavelength in aerosol optical instruments, indole + OH SOA k values range between 0.03 and 0.05 for low-NO_x and higher NO_x conditions, with the measured largest value of 0.12 in the OFR measurements. Indole + O_3 SOA k values at 405 nm range from $0.02 - 0.05$, while indole + NO_3 SOA k values range from $0.04 - 0.08$. This is comparable to k values observed for products of reaction of NO_3 with non-soluble tar balls (Li et al. 2020b). For reference, at 405 nm, α-pinene + OH (biogenic SOA), naphthalene + OH + NO_x (anthropogenic SOA), and guaiacol + OH (biomass burning SOA) k values are orders of magnitude smaller, reported to be between $0.0002 - 0.001$, $0.001 - 0.018$, and 0.0005-0.001, respectively (He et al. 2022; Lambe et al. 2013; Moise, Flores, and Rudich 2015). On the other hand, k values measured in this work are comparable with strongly absorbing biomass burning OA reported in our earlier study (Li et al. 2020b). This makes indole SOA a uniquely efficient type of BrC compared to SOA produced from other precursors. In fact, indole SOA k values are most similar to those from highly absorbing Humic-like substances (HULIS) such as Suwannee River Fulvic Acid (SRFA) with values between $0.036 - 0.056$ (Flores et al. 2014). Furthermore, other biogenic SOA formed from nitrate radical oxidation (isoprene, α-humulene, β-caryophyllene, etc.) have been found to have a negligible k values at 405 nm (He et al. 2021), highlighting the uniquely efficient light absorption of indole + NO_3 SOA.

3.3. Chromophoric compounds in SOA

HPLC-PDA-HRMS analysis was used to identify individual chromophores in the indole + O_3 and indole + NO_3 SOA samples, extending our previous study of the indole + OH SOA system (Montoya-Aguilera et al. 2017). These experiments were not done for the indole + OH + NO_x SOA. In the case of indole + NO_3 SOA, which had a non-monotonic dependence of *MAC* on RH, this analysis was done for SOA produced under dry (<2% RH), 25%, and 50% RH conditions. A representative HPLC-PDA chromatograph is shown in Figure 5. Table S2 lists the individual chromophores and their proposed structures based on elemental formulas obtained from the HRMS analysis and reference UV-Vis absorption
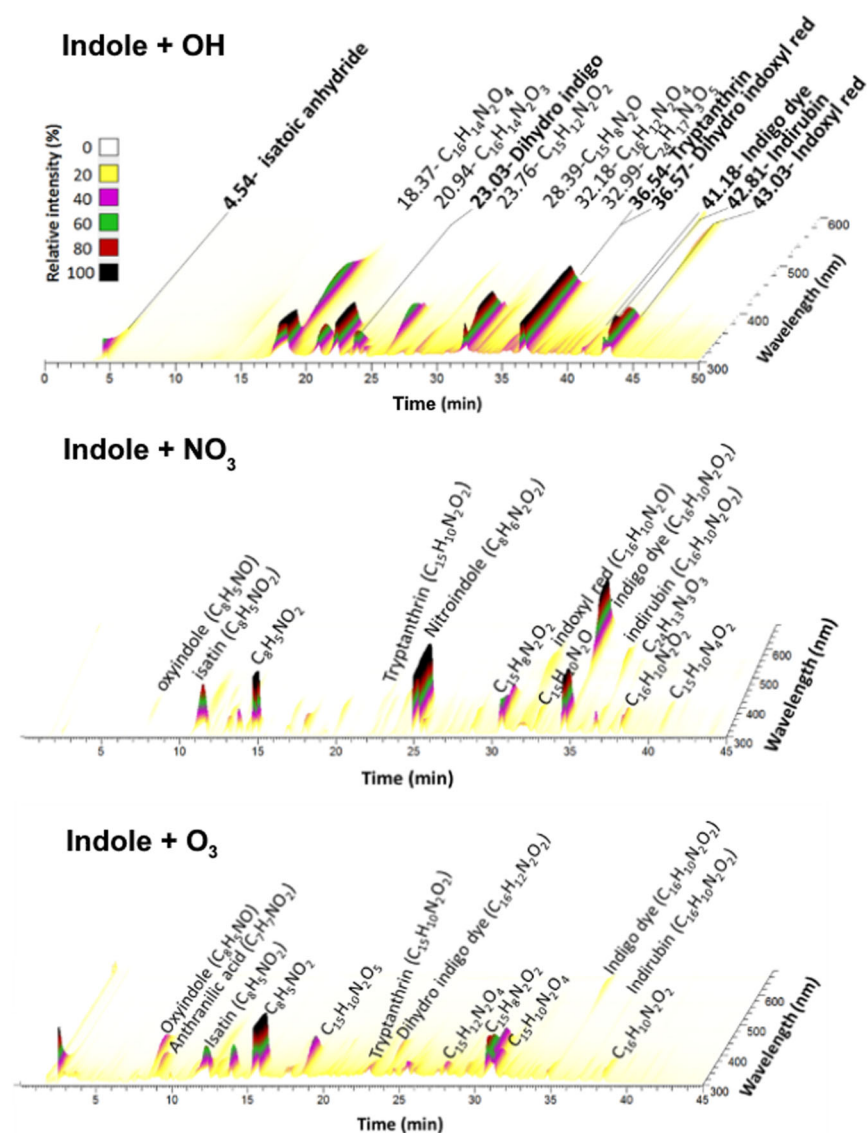
Figure 5. An HPLC-PDA chromatogram acquired with column A for indole + O₃ SOA sample and indole + NO₃ SOA sample generated in the smog chamber at low relative humidity (<2% RH). The PDA absorbance is plotted as a function of both retention time and wavelength. Peaks are labeled by their proposed assignment (Table S2). For comparison, the HPLC-PDA chromatogram for indole + OH SOA is reproduced from our previous work (Montoya-Aguilera et al. 2017).

spectra from literature. Altogether, 28 individual compounds can be tentatively identified, including 6 monomers, 20 dimers, and 2 trimers. Monomeric compounds are especially relevant to this discussion, as the dimers and trimers are much less likely to form under lower, atmospherically relevant concentrations of indole in the atmosphere. A noteworthy finding is that the mass absorption coefficients of indole + NO₃ SOA are relatively insensitive to the starting indole mixing ratio (Figure S1), which may suggest that the dimers are produced by particle-phase chemistry as opposed to gas-phase chemistry.

Three chromophores (tryptanthrin, indigo dye, and indirubin) are observed in all three SOA types, and seven additional chromophores are shared by two

SOA types. Indigo dye, while not unique to the indole + NO₃ SOA, is the chromophore contributing to the prominent peak at 600 nm in the indole + NO₃ SOA absorbance spectrum (Figure 1d).

As already mentioned, the k values for indole + NO₃ SOA exhibit a non-monotonic dependence on RH. To examine this further, the most abundant compounds absorbing between 350 – 450 nm were identified by examining the correlation between chromatographic peaks detected by both PDA and mass spectroscopy and the normalized intensities of that peak (Figure 6). It is important to note that this set of experiments was carried out later in the project using a shorter chromatography column (Column B), and, thus, the retention times of the identified compounds do not overlap with
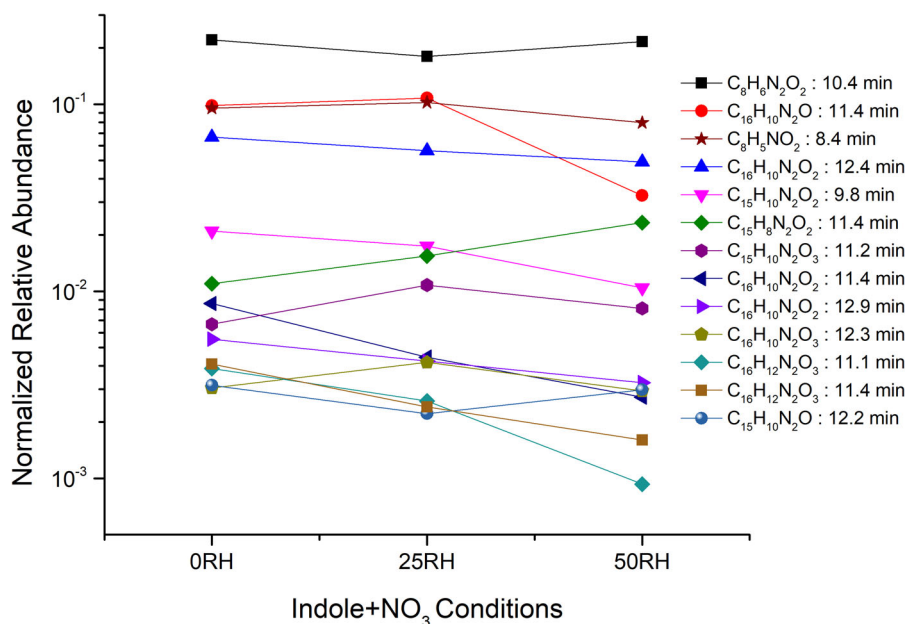
Figure 6. Indole + NO$_3$ SOA chromophore abundances when prepared under dry (<2%), 25%, and 50% RH conditions. Some chromophores exhibit a monotonic dependence on RH, whereas others do not. The y-axis shows the normalized relative abundance of the assigned peak and is displayed on a log$_{10}$ scale. Normalization was done by dividing the assigned peak intensity by the sum of assigned peak intensities for each indole + NO$_3$ condition. These data were acquired using column B (resulting in different retention times from those listed in Table S2 for column A).

those listed in Table S2. However, the order in which they elute is the same.

While the abundances of some of the detected chromophores, such as tryptanthrin (C$_{15}$H$_{10}$N$_2$O$_2$), exhibit a monotonic dependence on RH, some of them follow a non-monotonic trend similar to the k values. For example, nitroindole (C$_8$H$_6$N$_2$O$_2$) abundance in indole + NO$_3$ SOA decreases when RH changes from <2% to 25% but increases again when at 50% RH. Nitroindole is most likely responsible for the non-monotonic k value dependence, as it is the most abundant compound in indole + NO$_3$ SOA under all RH conditions, accounting for 20% of the total ion abundance. A chromophore that is unique to indole + NO$_3$ SOA (see Table S2), with an assigned chemical formula of C$_{15}$H$_{10}$N$_2$O, also follows this RH-dependence trend. Other chromophores follow the opposite trend with abundance increasing from <2% to 25% RH, then decreasing from 25% RH to 50% RH, e.g., for indoxyl red (C$_{16}$H$_{10}$N$_2$O).

The ToF-AMS results from the OFR experiments for the indole + NO$_3$ SOA also exhibited non-monotonic trends of various molecular fragments as a function of RH (Figure S6). The AMS chemical families that showed a similar RH dependence to the measured k values were the C$_x$H$_y$O$^+$ and C$_x$H$_y$O$_z^+$ (Figure S6). In contrast, the NO$^+$ and C$_x$H$_y^+$ families followed the opposite RH dependence to the k values. Based on AMS data, the NO$^+$ to NO$_2^+$ ratios for

indole + NO$_3$ SOA generated at <2%, 25%, 51%, and 76% RH were 4.3, 5.9, 5.6, and 6.9 respectively. While the NO$^+$ to NO$_2^+$ ratios have not been systematically measured for heterocyclic compounds, they are similar to the values reported for organonitrates ($\sim$3–5), and higher than values reported for ammonium nitrate ($\sim$1.5–2.4) (Bruns et al. 2010; Farmer et al. 2010). Therefore, we do not think these results are affected by the presence of inorganic nitrate in the particles. While we do not have an explanation for the complex RH dependence of AMS peak abundances, the data suggest that at least two competing mechanisms operate, with one favoring dry conditions and the other favoring humidified conditions.

4. Conclusions and implications

This study has examined the light-absorbing properties of indole SOA formed through ozonolysis, photochemical OH oxidation in the presence and absence of NO$_x$, and dark nitrate radical oxidation. In all cases, the SOA contains strong chromophores, resulting in high imaginary refractive index (k ranging from 10^{-2} to 10^{-1} at 405 nm) values comparable to those for humic-like substances and at least an order of magnitude larger than k values of SOA produced from other biogenic and anthropogenic sources. This means that in areas with elevated indole emissions, such as downwind of animal husbandry facilities, this

type of SOA can contribute to visibility degradation. It will be of interest to test this assumption with modeling studies of strong agricultural emissions using the data obtained in this work. It would also be of interest to directly observe indole oxidation products under these conditions. To aid in detection, Figure S7 provides full ToF-AMS spectra of OFR-generated indole + NO_3 SOA.

This is one of very few studies that examine the effect of RH on the optical properties of SOA. Both gas-phase and particle-phase processes leading to SOA formation, and aging can be affected by the presence of water vapor. Gaseous water molecules are known to react with Criegee intermediates formed in ozonolysis (Chao et al. 2015; Neeb et al. 1997), with a strong effect on particle nucleation and chemical composition (Bonn, Schuster, and Moortgat 2002; Zhao et al. 2015). Water molecules partitioned into aerosol particles can slowly hydrolyze organonitrates formed during NO_3 and OH/NO_x oxidation (Bean and Hildebrandt Ruiz 2016; Liu et al. 2012; Takeuchi and Ng 2019) and ester hydroperoxides produced from reactions of Criegee intermediates with organic acids (Zhao et al. 2018). RH can also have an indirect effect on SOA formation chemistry through its effect on particle viscosity, which strongly affects the size distribution and composition of SOA particles (Reid et al. 2018; Shiraiwa et al. 2013). Finally, the particle acidity is strongly RH-dependent, which could affect the chemistry of products derived from indole due to the presence of a basic -N(H)- group in these molecules. It is not clear whether the complex RH dependence for the absorption coefficient of indole + NO_3 SOA is driven by gas-phase or particle-phase processes. This represents an important gap in our understanding of these complex RH effects as the wall losses of gases in smog chambers strongly depend on RH (Huang et al. 2018). We hope that this work will prompt further studies into the RH-dependent mechanism of nitration of atmospherically-relevant aromatic and heterocyclic aromatic compounds over a wider range of oxidation conditions (e.g., at lower VOC concentrations and under conditions that minimize wall loss effects).

Disclosure statement

No potential conflict of interest was reported by the authors.

Author contributions
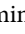
YR and SAN designed the experiments; JM, NNA, LTF, and VJB did the smog chamber experiments; QF did the OFR experiments; PL, JL, AL, and VJB recorded off-line mass-spectrometric data; JM, QF and VJB analyzed the data and wrote the manuscript; all authors edited the manuscript.

ORCID

Vahe J. Baboomian   http://orcid.org/0000-0002-7274-7109
Quanfu He   http://orcid.org/0000-0002-3229-8206
Julia Montoya-Aguilera   http://orcid.org/0000-0003-2272-0976
Nabila Ali   http://orcid.org/0000-0002-3698-8271
Lauren T. Fleming   http://orcid.org/0000-0001-6495-6261
Peng Lin   http://orcid.org/0000-0002-3567-7017
Alexander Laskin   http://orcid.org/0000-0002-7836-8417
Julia Laskin   http://orcid.org/0000-0002-4533-9644
Yinon Rudich   http://orcid.org/0000-0003-3149-0201
Sergey A. Nizkorodov   http://orcid.org/0000-0003-0891-0052

References

Andreae, M. O., and A. Gelencser. 2006. Black carbon or brown carbon? The nature of light-absorbing carbonaceous aerosols. *Atmos. Chem. Phys.* 6 (10):3131–48. doi:10.5194/acp-6-3131-2006.

Atkinson, R., E. C. Tuazon, J. Arey, and S. M. Aschmann. 1995. Atmospheric and indoor chemistry of gas-phase indole, quinoline, and isoquinoline. *Atmos. Environ.* 29 (23):3423–32. doi:10.1016/1352-2310(95)00103-6.

Baeyer, A., and V. Drewsen. 1882. Darstellung von Indigblau aus Orthonitrobenzaldehyd. *Ber. Dtsch. Chem. Ges.* 15 (2):2856–64. doi:10.1002/cber.188201502274.

Bean, J. K., and L. Hildebrandt Ruiz. 2016. Gas-particle partitioning and hydrolysis of organic nitrates formed from the oxidation of alpha-pinene in environmental chamber experiments. *Atmos. Chem. Phys.* 16 (4):2175–84. doi:10.5194/acp-16-2175-2016.

Bonn, B., G. Schuster, and G. K. Moortgat. 2002. Influence of water vapor on the process of new particle formation during monoterpene ozonolysis. *J. Phys. Chem. A* 106 (12):2869–81. doi:10.1021/jp012713p.

Bruns, E. A., V. Perraud, A. Zelenyuk, M. J. Ezell, S. N. Johnson, Y. Yu, D. Imre, B. J. Finlayson-Pitts, and M. L. Alexander. 2010. Comparison of FTIR and particle mass spectrometry for the measurement of particulate organic nitrates. *Environ. Sci. Technol.* 44 (3):1056–61. doi:10.1021/es9029864.

Chao, W., J.-T. Hsieh, C.-H. Chang, and J. J.-M. Lin. 2015. Direct kinetic measurement of the reaction of the simplest Criegee intermediate with water vapor. *Science* 347 (6223):751–4.

Chen, D., M. Rojas, B. H. Samset, K. Cobb, A. Diongue Niang, P. Edwards, S. Emori, S. H. Faria, E. Hawkins, P. Hope, et al. 2021. 2021: Framing, context, and methods. In *Climate Change 2021: The Physical Science Basis. Contribution of Working Group I to the Sixth Assessment Report of the Intergovernmental Panel on Climate Change*, eds. V. Masson-Delmotte, P. Zhai, A. Pirani, S. L. Connors, C. Péan, S. Berger, N. Caud, Y. Chen, L. Goldfarb, M. I. Gomis, M., et al., Cambridge University Press, Cambridge, United Kingdom, 147–286.

Coggon, M. M., G. I. Gkatzelis, B. C. McDonald, J. B. Gilman, R. H. Schwantes, N. Abuhassan, K. C. Aikin, M. F. Arend, T. A. Berkoff, S. S. Brown, et al. 2021. Volatile chemical product emissions enhance ozone and modulate urban chemistry. *Proc. Natl. Acad. Sci. U. S. A.* 118 (32):e2026653118.

Cui, Y. M., A. L. Frie, J. H. Dingle, S. Zimmerman, I. Frausto-Vicencio, F. Hopkins, and R. Bahreini. 2021. Influence of ammonia and relative humidity on the formation and composition of secondary brown carbon from oxidation of 1-methylnaphthalene and longifolene. *ACS Earth Space Chem.* 5 (4):858–69. doi:10.1021/acsearthspacechem.0c00353.

Farmer, D. K., A. Matsunaga, K. S. Docherty, J. D. Surratt, J. H. Seinfeld, P. J. Ziemann, and J. L. Jimenez. 2010. Response of an aerosol mass spectrometer to organonitrates and organosulfates and implications for atmospheric chemistry. *Proc. Natl. Acad. Sci. U S A.* 107 (15):6670–5. doi:10.1073/pnas.0912340107.

Flores, J. M., R. A. Washenfelder, G. Adler, H. J. Lee, L. Segev, J. Laskin, A. Laskin, S. A. Nizkorodov, S. S. Brown, and Y. Rudich. 2014. Complex refractive indices in the near-ultraviolet spectral region of biogenic secondary organic aerosol aged with ammonia. *Phys. Chem. Chem. Phys.* 16 (22):10629–42. doi:10.1039/c4cp01009d.

Friedel, R. A., and M. Orchin. 1951. *Ultraviolet spectra of aromatic compounds*. New York: John Wiley & Sons, Inc., 579. spectra included.

Gentner, D. R., E. Ormeño, S. Fares, T. B. Ford, R. Weber, J. H. Park, J. Brioude, W. M. Angevine, J. F. Karlik, and A. H. Goldstein. 2014. Emissions of terpenoids, benzenoids, and other biogenic gas-phase organic compounds from agricultural crops and their potential implications for air quality. *Atmos. Chem. Phys.* 14 (11):5393–413. doi:10.5194/acp-14-5393-2014.

Hallquist, M., J. C. Wenger, U. Baltensperger, Y. Rudich, D. Simpson, M. Claeys, J. Dommen, N. M. Donahue, C. George, A. H. Goldstein, et al. 2009. The formation, properties and impact of secondary organic aerosol: Current and emerging issues. *Atmos. Chem. Phys.* 9 (14):5155–236. doi:10.5194/acp-9-5155-2009.

He, Q. F., N. Bluvshtein, L. Segev, D. Meidan, J. M. Flores, S. S. Brown, W. Brune, and Y. Rudich. 2018. Evolution of the complex refractive index of secondary organic aerosols during atmospheric aging. *Environ. Sci. Technol.* 52 (6):3456–65. doi:10.1021/acs.est.7b05742.

He, Q. F., C. L. Li, K. Siemens, A. C. Morales, A. P. S. Hettiyadura, A. Laskin, and Y. Rudich. 2022. Optical properties of secondary organic aerosol produced by photooxidation of naphthalene under NOx condition. *Environ. Sci. Technol.* 56 (8):4816–27.

He, Q. F., S. Tomaz, C. L. Li, M. Zhu, D. Meidan, M. Riva, A. Laskin, S. S. Brown, C. George, X. M. Wang, et al. 2021. Optical properties of secondary organic aerosol produced by nitrate radical oxidation of biogenic volatile organic compounds. *Environ. Sci. Technol.* 55 (5):2878–89. doi:10.1021/acs.est.0c06838.

Herrmann, H., T. Schaefer, A. Tilgner, S. A. Styler, C. Weller, M. Teich, and T. Otto. 2015. Tropospheric aqueous-phase chemistry: Kinetics, mechanisms, and its coupling to a changing gas phase. *Chem. Rev.* 115 (10):4259–334. doi:10.1021/cr500447k.

Hettiyadura, A. P. S., V. Garcia, C. L. Li, C. P. West, J. Tomlin, Q. F. He, Y. Rudich, and A. Laskin. 2021. Chemical composition and molecular-specific optical properties of atmospheric brown carbon associated with biomass burning. *Environ. Sci. Technol.* 55 (4):2511–21. doi:10.1021/acs.est.0c05883.

Hobbs, P. J., T. H. Misselbrook, and B. F. Pain. 1997. Characterisation of odorous compounds and emissions from slurries produced from weaner pigs fed dry feed and liquid diets. *J. Sci. Food Agric.* 73 (4):437–45. doi:10.1002/(SICI)1097-0010(199704)73:4<437::AID-JSFA748>3.0.CO;2-7.

Hodzic, A., P. S. Kasibhatla, D. S. Jo, C. D. Cappa, J. L. Jimenez, S. Madronich, and R. J. Park. 2016. Rethinking the global secondary organic aerosol (SOA) budget: Stronger production, faster removal, shorter lifetime. *Atmos. Chem. Phys.* 16 (12):7917–41. doi:10.5194/acp-16-7917-2016.

Huang, Y. L., R. Zhao, S. M. Charan, C. M. Kenseth, X. Zhang, and J. H. Seinfeld. 2018. Unified theory of vapor-wall mass transport in Teflon-walled environmental chambers. *Environ. Sci. Technol.* 52 (4):2134–42. doi:10.1021/acs.est.7b05575.

Jo, S. H., K. H. Kim, B. H. Jeon, M. H. Lee, Y. H. Kim, B. W. Kim, S. B. Cho, O. H. Hwang, and S. S. Bhattacharya. 2015. Odor characterization from barns and slurry treatment facilities at a commercial swine facility in South Korea. *Atmos. Environ.* 119:339–47. doi:10.1016/j.atmosenv.2015.08.064.

Kasthuriarachchi, N. Y., L. H. Rivellini, X. Chen, Y. J. Li, and A. K. Y. Lee. 2020. Effect of relative humidity on secondary brown carbon formation in aqueous droplets. *Environ. Sci. Technol.* 54 (20):13207–16. doi:10.1021/acs.est.0c01239.

Lack, D. A., R. Bahreini, J. M. Langridge, J. B. Gilman, and A. M. Middlebrook. 2013. Brown carbon absorption linked to organic mass tracers in biomass burning particles. *Atmos. Chem. Phys.* 13 (5):2415–22. doi:10.5194/acp-13-2415-2013.

Lambe, A., P. Massoli, X. Zhang, M. Canagaratna, J. Nowak, C. Daube, C. Yan, W. Nie, T. Onasch, J. Jayne, et al. 2017. Controlled nitric oxide production via O(^{1}D) + N$_2$O reactions for use in oxidation flow reactor studies. *Atmos. Meas. Tech.* 10 (6):2283–98. doi:10.5194/amt-10-2283-2017.

Lambe, A. T., C. D. Cappa, P. Massoli, T. B. Onasch, S. D. Forestieri, A. T. Martin, M. J. Cummings, D. R. Croasdale, W. H. Brune, D. R. Worsnop, et al. 2013.

Relationship between oxidation level and optical properties of secondary organic aerosol. *Environ. Sci. Technol.* 47 (12):6349–57. doi:10.1021/es401043j.

Lang-Yona, M., Y. Rudich, E. Segre, E. Dinar, and A. Abo-Riziq. 2009. Complex refractive indices of aerosols retrieved by continuous wave-cavity ring down aerosol spectrometer. *Anal. Chem.* 81 (5):1762–9. doi:10.1021/ac8017789.

Laskin, A., J. Laskin, and S. A. Nizkorodov. 2015. Chemistry of atmospheric brown carbon. *Chem. Rev.* 115 (10):4335–82. doi:10.1021/cr5006167.

Le, P. D., A. J. A. Aarnink, N. W. M. Ogink, P. M. Becker, and M. W. A. Verstegen. 2005. Odour from animal production facilities: Its relationship to diet. *Nutr. Res. Rev.* 18 (1):3–30. doi:10.1079/NRR200592.

Li, C. L., Q. F. He, Z. Fang, S. S. Brown, A. Laskin, S. R. Cohen, and Y. Rudich. 2020a. Laboratory Insights into the diel cycle of optical and chemical transformations of biomass burning brown carbon aerosols. *Environ. Sci. Technol.* 54 (19):11827–37. doi:10.1021/acs.est.0c04310.

Li, C. L., Q. F. He, A. P. S. Hettiyadura, U. Kafer, G. Shmul, D. Meidan, R. Zimmermann, S. S. Brown, C. George, A. Laskin, et al. 2020b. Formation of secondary brown carbon in biomass burning aerosol proxies through NO3 Radical Reactions. *Environ. Sci. Technol.* 54 (3):1395–405. doi:10.1021/acs.est.9b05641.

Lin, P., P. K. Aiona, Y. Li, M. Shiraiwa, J. Laskin, S. A. Nizkorodov, and A. Laskin. 2016. Molecular characterization of brown carbon in biomass burning aerosol particles. *Environ. Sci. Technol.* 50 (21):11815–24. doi:10.1021/acs.est.6b03024.

Lin, P., J. M. Liu, J. E. Shilling, S. M. Kathmann, J. Laskin, and A. Laskin. 2015. Molecular characterization of brown carbon (BrC) chromophores in secondary organic aerosol generated from photo-oxidation of toluene. *Phys. Chem. Chem. Phys.* 17 (36):23312–25. doi:10.1039/C5CP02563J.

Liu, P. F., N. Abdelmalki, H. M. Hung, Y. Wang, W. H. Brune, and S. T. Martin. 2015. Ultraviolet and visible complex refractive indices of secondary organic material produced by photooxidation of the aromatic compounds toluene and m-Xylene. *Atmos. Chem. Phys.* 15 (3):1435–46. doi:10.5194/acp-15-1435-2015.

Liu, S., J. E. Shilling, C. Song, N. Hiranuma, R. A. Zaveri, and L. M. Russell. 2012. Hydrolysis of organonitrate functional groups in aerosol particles. *Aerosol Sci. Technol* 46 (12):1359–69. doi:10.1080/02786826.2012.716175.

McDonald, B. C., J. A. de Gouw, J. B. Gilman, S. H. Jathar, A. Akherati, C. D. Cappa, J. L. Jimenez, J. Lee-Taylor, P. L. Hayes, S. A. McKeen, et al. 2018. Volatile chemical products emerging as largest petrochemical source of urban organic emissions. *Science* 359 (6377):760–4. doi:10.1126/science.aaq0524.

Mitra, K., H. R. Mishra, X. Y. Pei, and R. K. Pathak. 2022. Secondary organic aerosol (SOA) from photo-oxidation of toluene: 1 influence of reactive nitrogen, acidity and water vapours on optical properties. *Atmosphere* 13 (7):1099. doi:10.3390/atmos13071099.

Moise, T., J. M. Flores, and Y. Rudich. 2015. Optical properties of secondary organic aerosols and their changes by chemical processes. *Chem. Rev.* 115 (10):4400–39. doi:10.1021/cr5005259.

Montoya-Aguilera, J., J. R. Horne, M. L. Hinks, L. T. Fleming, V. Perraud, P. Lin, A. Laskin, J. Laskin, D. Dabdub, and S. A. Nizkorodov. 2017. Secondary organic aerosol from atmospheric photooxidation of indole. *Atmos. Chem. Phys.* 17 (18):11605–21. doi:10.5194/acp-17-11605-2017.

Neeb, P., F. Sauer, O. Horie, and G. K. Moortgat. 1997. Formation of hydroxymethyl hydroperoxide and formic acid in alkene ozonolysis in the presence of water vapor. *Atmos. Environ* 31 (10):1417–23. doi:10.1016/S1352-2310(96)00322-6.

Osaka, N., A. Miyazaki, and N. Tanaka. 2018. Emissions of volatile organic compounds from a Swine shed. *ajae.* 12 (2):178–91. doi:10.5572/ajae.2018.12.2.178.

Parker, D. B., J. Gilley, B. Woodbury, K. H. Kim, G. Galvin, S. L. Bartelt-Hunt, X. Li, and D. D. Snow. 2013. Odorous VOC emission following land application of swine manure slurry. *Atmos. Environ* 66:91–100. doi:10.1016/j.atmosenv.2012.01.001.

Pluskal, T., S. Castillo, A. Villar-Briones, and M. Oresic. 2010. MZmine 2: Modular framework for processing, visualizing, and analyzing mass spectrometry-based molecular profile data. *BMC Bioinf.* 11:395. doi:10.1186/1471-2105-11-395.

Reid, J. P., A. K. Bertram, D. O. Topping, A. Laskin, S. T. Martin, M. D. Petters, F. D. Pope, and G. Rovelli. 2018. The viscosity of atmospherically relevant organic particles. *Nat. Commun.* 9:956. doi:10.1038/s41467-018-03027-z.

Riziq, A. A., C. Erlick, E. Dinar, and Y. Rudich. 2007. Optical properties of absorbing and non-absorbing aerosols retrieved by cavity ring down (CRD) spectroscopy. *Atmos. Chem. Phys.* 7 (6):1523–36. doi:10.5194/acp-7-1523-2007.

Saleh, R. 2020. From measurements to models: Toward accurate representation of brown carbon in climate calculations. *Curr. Pollution Rep.* 6 (2):90–104. doi:10.1007/s40726-020-00139-3.

Samburova, V., J. Connolly, M. Gyawali, R. L. N. Yatavelli, A. C. Watts, R. K. Chakrabarty, B. Zielinska, H. Moosmuller, and A. Khlystov. 2016. Polycyclic aromatic hydrocarbons in biomass-burning emissions and their contribution to light absorption and aerosol toxicity. *Sci. Total Environ.* 568:391–401. doi:10.1016/j.scitotenv.2016.06.026.

Shiraiwa, M., L. D. Yee, K. A. Schilling, C. L. Loza, J. S. Craven, A. Zuend, P. J. Ziemann, and J. H. Seinfeld. 2013. Size distribution dynamics reveal particle-phase chemistry in organic aerosol formation. *Proc. Natl. Acad. Sci. U. S. A.* 110 (29):11746–50. doi:10.1073/pnas.1307501110.

Siemens, K., A. Morales, Q. F. He, C. L. Li, A. P. S. Hettiyadura, Y. Rudich, and A. Laskin. 2022. Molecular Analysis of secondary brown carbon produced from the photooxidation of naphthalene. *Environ. Sci. Technol.* 56 (6):3340–53.

Takeuchi, M., and N. L. Ng. 2019. Chemical composition and hydrolysis of organic nitrate aerosol formed from hydroxyl and nitrate radical oxidation of alpha-pinene and beta-pinene. *Atmos. Chem. Phys.* 19 (19):12749–66. doi:10.5194/acp-19-12749-2019.

Washenfelder, R. A., J. M. Flores, C. A. Brock, S. S. Brown, and Y. Rudich. 2013. Broadband measurements of aerosol extinction in the ultraviolet spectral region. *Atmos. Meas. Tech.* 6 (4):861–77. doi:10.5194/amt-6-861-2013.

Weinstein, J., and G. M. Wyman. 1956. Spectroscopic studies on DYES. I. The association of indigo dyes in the solid phase. *J. Am. Chem. Soc.* 78 (11):2387–90. doi:10.1021/ja01592a012.

Zhao, R., C. M. Kenseth, Y. L. Huang, N. F. Dalleska, X. B. M. Kuang, J. R. Chen, S. E. Paulson, and J. H. Seinfeld. 2018. Rapid aqueous-phase hydrolysis of ester hydroperoxides arising from criegee intermediates and organic acids. *J. Phys. Chem. A* 122 (23):5190–201. doi:10.1021/acs.jpca.8b02195.

Zhao, Y., L. M. Wingen, V. Perraud, J. Greaves, and B. J. Finlayson-Pitts. 2015. Role of the reaction of stabilized Criegee intermediates with peroxy radicals in particle formation and growth in air. *Phys. Chem. Chem. Phys.* 17 (19):12500–14. doi:10.1039/c5cp01171j.

Zito, P., S. Dotterl, and M. Sajeva. 2015. Floral volatiles in a sapromyiophilous plant and their importance in attracting house fly pollinators. *J. Chem. Ecol.* 41 (4):340–9. doi:10.1007/s10886-015-0568-8.